SCIENTIFIC REP🗘RTS

OPEN

One-pot hydrothermal synthesis of CdS decorated CuS microflower-like structures for enhanced photocatalytic properties

Xiaolong Deng [iD], Chenggang Wang, Hongcen Yang, Minghui Shao, Shouwei Zhang, Xiao Wang, Meng Ding, Jinzhao Huang & Xijin Xu

CdS decorated CuS structures have been controllably synthesized through a one-pot hydrothermal method. The morphologies and compositions of the as-prepared samples could be concurrently well controlled by simply tuning the amount of CdCl$_2$ and thiourea. Using this strategy, the morphology of the products experienced from messy to flower-like morphologies with multiple porous densities, together with the phase evolution from pure CuS to the CdS/CuS composites. Serving as a photocatalyst, the samples synthesized with the addition of 1 mmol cadmium chloride and 3 mmol thiourea during synthetic process, showed the best photocatalytic activity, which could reach a maximum photocatalytic efficiency of 93% for methyl orange (MO) photodegradation after 150 min. The possible mechanism for the high photocatalytic efficiency of the sample was proposed by investigating the composition, surface area, structure, and morphology before and after photocatalytic reaction.

Semiconductor photocatalysis as a green technology for wastewater/organic contaminants treatment and green energy production has attracted considerable attention since Fujishima and Honda realized water splitting to generate hydrogen by using TiO$_2$ in 1972[1–4]. Since then, various photocatalysts, such as transition metal oxides[5–8], metal sulfides[9–12], heterojunctions[13–15], doping materials[16–18], composite structures[19, 20], have been synthesized to improve the photocatalytic activities. Among them, metal chalcogenides were considered to be promising photocatalytic candidates due to their unique properties, such as suitable band gap, ideal electronic band position and thus exhibiting excellent catalytic activities[10, 21, 22]. Particularly, copper sulfide (CuS) and cadmium sulfide (CdS) were widely investigated in the application of photocatalysis[4, 10, 23–26].

CuS could absorb visible light in the solar spectrum due to its narrow band gap of about 2.08 eV[4, 10, 27, 28] and the abundant raw materials on earth have made the photocatalysts syntheses inexpensive. Therefore, considerable attention and approaches have been paid to synthesize diverse shaped CuS. For instance, CuS microflowers composed of nanosheets were obtained by a one-pot sonochemical process and their versatile photocatalyst responses were investigated under natural light irradiation by Cao et al.[4]. Pradhan et al. has synthesized CuS submicro-spheres and nanotubes by a solution chemistry route and revealed that the synthetic conditions could affect the shape, size and structure of CuS and thus its photocatalytic activities[10]. However, using CuS as photocatalyst alone was similar to most single semiconductor photocatalyst which encounters low photocatalytic activity[3, 29]. Therefore, many efforts have been made to improve the photocatalytic properties of CuS-based photocatalysts. For example, metal ions doped CuS with enhanced visible light photocatalytic activity on dyes degradation was prepared by Hosseinpour et al.[28]. In addition, CuS loaded on metal sulfides including ZnS[30, 31], CdS[29], even ZnS-CuS-CdS composite[21], were studied and found possessing high photocatalytic activity toward H$_2$ generation under visible light irradiation. So far, exploring more efficient CuS-based photocatalyst is still highly desirable because few studies based on CuS as the host coupled with metal sulfides are conducted.

Although the rapid recombination rate of photogenerated electron-hole pairs for pure CdS on one hand limits its photocatalytic activity owing to its band energies[22, 29, 32–36], the serious photocorrosion of CdS is another

School of Physics and Technology, University of Jinan, 336 Nanxin Zhuang West Road, Jinan, 250022, Shandong Province, People's Republic of China. Correspondence and requests for materials should be addressed to J.H. (email: ss_huangjinzhao@ujn.edu.cn) or X.X. (email: sps_xuxj@ujn.edu.cn)

Sample	CdCl$_2$·2.5H$_2$O	Thiourea	PEG	Cu(NO$_3$)$_2$·3H$_2$O	Temperature (°C)	Time (h)
Cd-0	0 mmol	3 mmol				
Cd-0.5	0.5 mmol	3 mmol				
Cd-1	1 mmol	3 mmol				
Cd-2	2 mmol	3 mmol				
Cd-4	4 mmol	3 mmol	0.098 g	4 mmol	140	10
Cd-1-T4	1 mmol	4 mmol				
Cd-1-T6	1 mmol	6 mmol				
Cd-0-T6	0 mmol	6 mmol				

Table 1. The synthesis conditions for the preparation of samples

obstacle hindering its wide application as high-performance photocatalysts[34, 36]. But, CdS is still worthwhile to be used as a photocatalyst due to its narrow band gap of 2.4 eV, endowing it the extremely feasible feature to absorb light irradiation in visible light range[22, 24, 29]. Therefore, many efforts have been made to overcome the aforementioned disadvantages and various nanostructured CdS materials had been synthesized, such as nano-rods[23], nanoflowers[23], nanospheres[24], nanotubes[37], nanowires[38, 39], nanosheets[40], nanocone and nanofrustum[41] *etc*. Recently, the photocatalytic efficiency of CdS could be further improved by coupling it with other materials to form hybrid structures, such as WS$_2$[22], ZnO[33], Al$_2$O$_3$[33], ZnS-CuS[21], CuS[29], TiO$_2$[42, 43], graphene[32], histidine[44] *etc*, due to the effective separation of photogenerated electron-hole pairs. Therefore, it is reasonable to deduce that the structure hybridization of CuS and CdS could award us distinctly improved photocatalytic activities by extending light absorption of solar spectrum[29, 33]. In this sense, the facile preparation of high quality CdS loaded CuS heterostructure with precisely controlled morphologies and compositions and systematically investigate its photodegradation efficiency is very intriguing and important.

In this work, CdS decorated CuS photocatalysts were rationally designed and controllably synthesized *via* a facile one-pot hydrothermal method. The effect of the CdCl$_2$ and the concentration of thiourea precursor on the structures and morphologies of as-prepared samples were systematically investigated by different characterization techniques. The photocatalytic activities of the as-prepared samples over methyl orange (MO) degradations under visible light irradiation were performed and a possible reaction mechanism was proposed by evaluating the post-photodegradation analysis.

Experimental

Synthesis of CdS decorated CuS photocatalysts.
All chemical reagents were of analytical grade and used without further purification, which purchased from Sinopharm Chemical Reagent Co., Ltd. (SCRC, China). Typically, a certain amount of cadmium chloride (CdCl$_2$·2.5H$_2$O), 3 mmol thiourea and 0.098 g polyethylene glycol (PEG, M$_w$ = 2000) were dissolved into 80 mL deionized water by vigorously magnetic stirring for 10 min. Then, 4 mmol copper (II) nitrate trihydrate (Cu(NO$_3$)$_2$·3H$_2$O) was added into the solution followed by magnetically stirring for 1 hour to form homogeneous solution. After that, the solution was transferred into 100 mL Teflon-lined stainless steel autoclave. Thereafter, the sealed autoclave was kept at 140 °C for 10 hours, followed by cooling down to room temperature naturally. Subsequently, the as-prepared precipitates were collected by centrifugation and washed with deionized water and ethanol for several times. Finally, the products were obtained after drying the precipitants at 60 °C for 12 hours in a vacuum oven. The samples were named as Cd-0, Cd-0.5, Cd-1, Cd-2, and Cd-4 with the amount of CdCl$_2$·2.5H$_2$O of 0, 0.5, 1, 2, and 4 mmol, respectively. For comparison, another three samples (Cd-1-T4, Cd-1-T6, and Cd-0-T6) were prepared by changing the amount of chemical reagents while keeping other conditions the same. All the preparation conditions of the samples are listed in Table 1.

Characterization.
X-ray powder diffraction (XRD) patterns of as-prepared samples were recorded by a German X-ray diffractiometer (D8-Advance, Bruker AXS, Inc., Madsion, WI, USA) equipped with Cu K_α radiation (λ = 0.15406 nm). The morphologies of the samples were observed by a field emission scanning electron microscope (FESEM, FEI Quanta FEG250, FEI, Hillsboro, USA) and transmission electron microscope (TEM, HEOL-200CX, JEOL, Tokyo, Japan). High-resolution TEM images were also investigated with a field transmission electron microscope (Tecnai G2 F20 S-TWIN, FEI, Hillsboro, USA). The X-ray photoelectron spectroscopy (XPS) was collected on the Thermo ESCALAB 250XI electron spectrometer equipped with Al K_α X-ray radiation ($h\nu$ = 1486.6 eV) as the source for excitation (ThermoFisher Scientific, Waltham, MA USA). The Brunauer–Emmett–Teller (BET) specific surface areas of as-prepared samples were measured by N$_2$ adsorption–desorption isotherm with a Quantachrome NOVAtouch LX4 apparatus (Quantachrome Instruments, South San Francisco, CA, USA).

Photocatalytic measurement.
The photocatalytic properties of as-prepared samples were characterized by a UV-vis spectrophotometer (TU-1901, Beijing Purkinje General Instrument Co., Ltd, Beijing, China) at room temperature in air under visible light irradiation, which was similar to previous reports[8, 16]. The visible light was generated by a 500 W Xe lamp equipped with a cutoff filter ($\lambda \geq$ 420 nm) to remove the UV part. A typical process was carried out as follows: 30 mg products were dispersed into 50 ml of 10 mg/L methyl orange (MO) aqueous solution. Then, the suspension was kept in dark for 30 min with magnetic stirring to reach adsorption-desorption equilibrium of MO on the surface of as-grown samples. After a given irradiation time
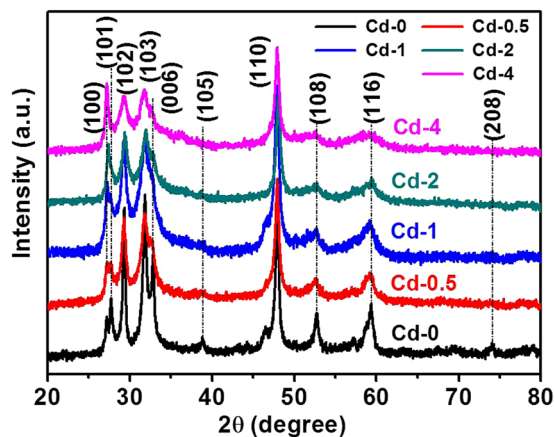
Figure 1. XRD patterns of as-prepared samples with various amounts of CdCl$_2$·2.5H$_2$O contents (Cd-0, Cd-0.5, Cd-1, Cd-2, and Cd-4) accompanying with the same other conditions.
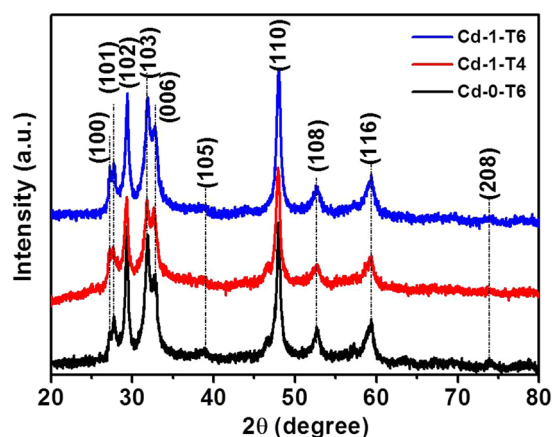

Figure 2. XRD patterns of as-grown samples by changing the amounts of CdCl$_2$·2.5H$_2$O and thiourea contents (Cd-1-T6, Cd-1-T4, and Cd-0-T6).

interval, ca. 3 mL suspension was transferred into the centrifuge tube to separate the powders and solution for the purpose of UV-vis spectra test. The concentration of MO was evaluated by measuring the absorbance properties at 464 nm in UV-vis spectra, which was used to illuminate the photocatalytic properties of as-prepared samples.

Results and Discussion

Structural and morphological characterization. XRD patterns of the as-prepared samples in Figs 1 and 2 show that all the peaks can be perfectly indexed into hexagonal CuS phase (JCPDS No. 65–3556). No other characteristic peaks could be found for all the samples, demonstrating their high crystalline purity and lower-level loading content of CdS on CuS. The only differences observed from these patterns were the intensity increase of (100) peak and the intensity decrease of (101) and (006) peaks, which could be ascribed to the addition of Cl$^-$ ions and the amount change of thiourea during the synthetic process that result in a tiny stoichiometry vary of the copper sulfides[45]. However, the phase and composition of the as-prepared samples keep almost unchanged with the addition of CdCl$_2$ and thiourea during the preparation process.

Sample Cd-0 in Fig. 3a presents the hierarchical structures consisted of nanofibers, spheres, and flake-like morphology, illustrating the uncontrollable morphologies manner of the sample synthesized without the existence of CdCl$_2$. Interestingly, after addition CdCl$_2$ (sample Cd-0.5), the morphology transformed into flower-like structure with inhomogeneous sizes and thin petals that composed of compact nanosheets, as depicted in Fig. 3b. Further increasing the amount of CdCl$_2$ (sample Cd-1) results in the formation of compact microflower-like structure with porous petals (Fig. 3c). Then, the compact flowers evolved into loosened structures accompanied by the decrease of porosities with further CdCl$_2$ content increasing (sample Cd-2, Fig. 3d). Finally, the morphology transformation completed with a result of assembling the nonporous and thick sheets together to form the heterogeneous structure for sample Cd-4 (Fig. 3e). In order to investigate the element distribution of the as-prepared samples, the energy dispersive X-ray spectroscopy (EDS) elemental mappings of two typical products Cd-1 and Cd-4 were recorded (Fig. 4). The results show that S, Cu and Cd elements are homogeneously distributed throughout the flowers. Furthermore, the effect of thiourea used on the morphology of the as-prepared
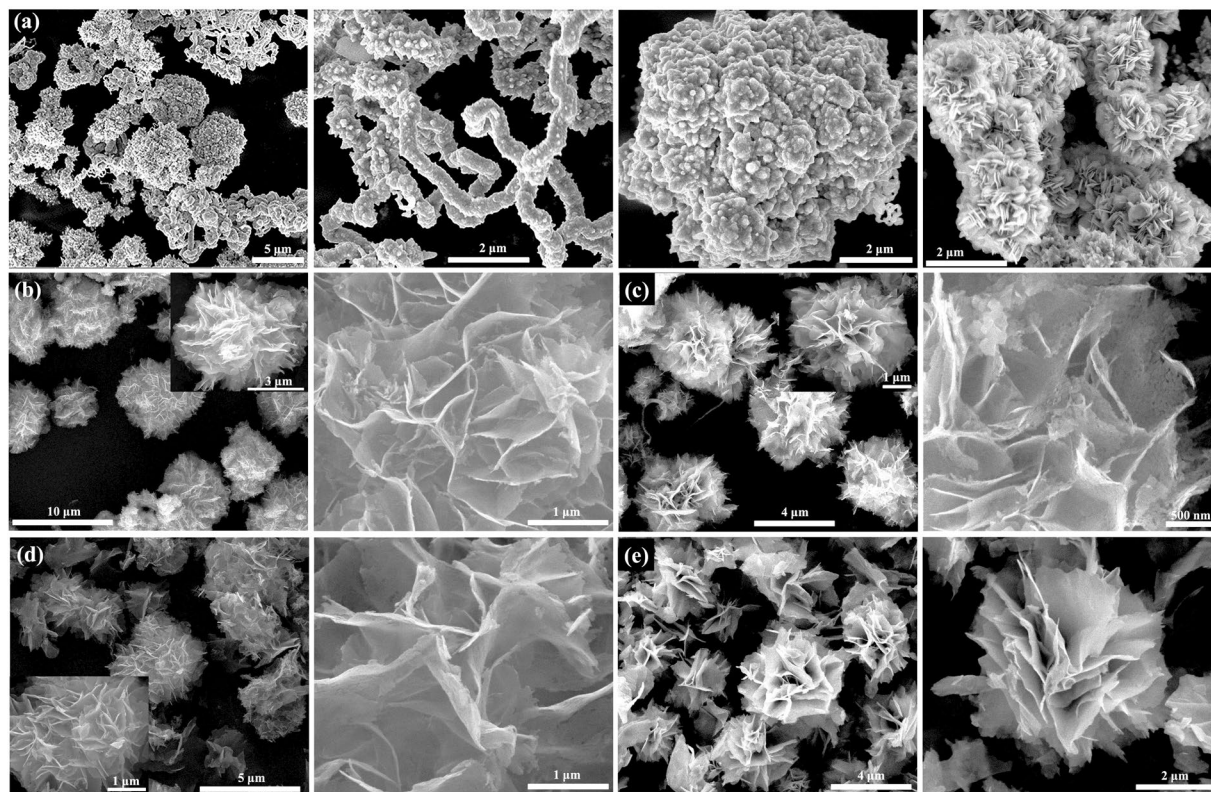
Figure 3. SEM images of as-prepared samples with different amount of Cd contents by keeping all other synthetic conditions fixed: (**a**) Cd-0, (**b**) Cd-0.5, (**c**) Cd-1, (**d**) Cd-2, and (**e**) Cd-4.
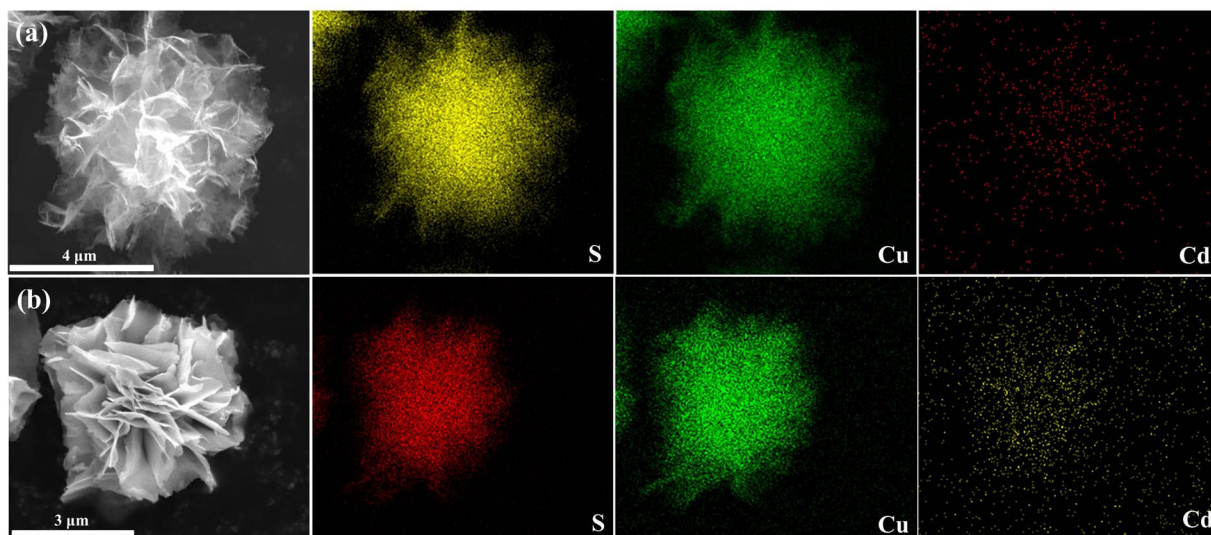

Figure 4. Typically elemental mapping images of Cd-1 (**a**) and Cd-4 (**b**) samples.

samples was investigated. As shown in Fig. 5, by fixing the $CdCl_2$ content (1 mmol) during the synthetic process, the porosity was disappeared with the increment use of thiourea (Fig. 5a, sample Cd-1-T4) and the sheets forming the petals became thicker as seen from the magnified SEM image (inset of Fig. 5a). After further increasing the amount of thiourea (Cd-1-T6, Fig. 5b) the flower becomes more compact and the petals grows even thicker with the disappearance of porosity. For comparison, the sample using 6 mmol thiourea without $CdCl_2$ addition (Cd-0-T6) was prepared and its SEM morphology was presented in Fig. 5c and d. It can be seen that fibers and irregular particles were formed which was quite different from that of Cd-0. Taken together, these results demonstrated that both thiourea and Cl^- anions from $CdCl_2$ addition (see Supporting Information Fig. SI-1)
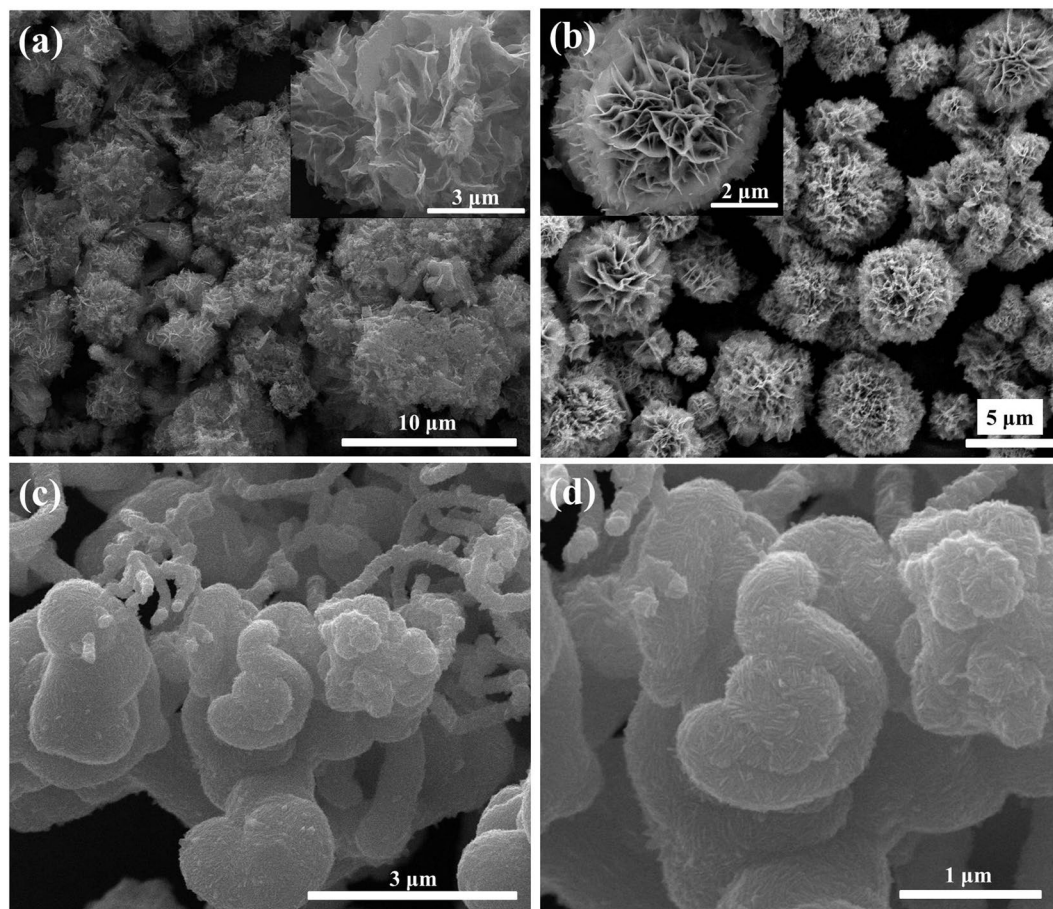
Figure 5. SEM observations of as-synthesized samples: (**a**) Cd-1-T4, (**b**) Cd-1-T6, and (**c,d**) Cd-0-T6.

played important roles in regulating the morphology of the as-prepared samples, in well agreement with previous reports[45–49].

TEM observation was further used to investigate the details of the as-prepared products. Figure 6a and b show that microflower structures with porous thin petals for Cd-1 and thick petals with a lower porous density for sample Cd-2 in Fig. 6c and d are observed, respectively. Figure 6e and f clearly confirm the existence of CdS particles deposited on the surface of CuS, and the distance between two crystal lattice fringes are 0.322 nm (CuS (101)) and 0.336 nm (CdS (002)) consisting with previously reported result[29]. In addition, the particle density in sample Cd-2 is higher than that of Cd-1, indicating more CdS particles were formed. Moreover, the thickness of the petals for Cd-1-T4 get thicker and the porosity drastically decreases (Fig. 6g and h), while the porosity almost disappears and the petals developed more thickly for Cd-1-T6 as shown in Fig. 6i and j. All these TEM results are consistent with the aforementioned SEM observations.

The XPS spectra of the prepared samples were recorded further to confirm the composition and the elemental oxidation states, as depicted in Fig. 7. The survey scans show that all the main peaks could be indexed into Cu, S, and Cd elements for all samples though the intensities were different (see Supporting Information Fig. SI-2). Particularly, the Cd peaks could not be detected for samples Cd-0 and Cd-0-T6, in well agreement with the synthesis conditions, where the absence of Cd addition in the reaction solution. The two stronger peaks with an energy separation of 19.9 eV at around 932.0 eV and 951.9 eV from Cu 2p region in Fig. 7a and b, respectively, are in accordance with the binding energy peaks for Cu 2p3/2 and Cu 2p1/2, conforming the Cu oxidation state is Cu (II)[4, 29]. The weak shakeup satellite peaks at 943.0 eV and 962.8 eV are also indexed to Cu^{2+} ions, indicating the paramagnetic chemical state of Cu^{2+} ion[4, 8, 29]. The Cd 3d region (except for sample Cd-0-T6) in Fig. 7a and b could be fitted into two main peaks locating at 405 eV and 412 eV, which are assigned to the binding energies of Cd 3d5/2 and Cd 3d3/2, suggesting the existence of Cd^{2+} in CdS[22, 29, 50]. In terms of Cd-0-T6 in Fig. 6b, there is no peak observed in the high resolution Cd 3d XPS region, illustrating the non-existence of CdS, which agrees well with the preparation conditions. The core-level XPS spectra of S 2p show different behaviors among the samples as depicted in Fig. 7. For the samples without $CdCl_2$ addition (Cd-0 and Cd-0-T6), only two main peaks located at 162.3 eV (S 2p3/2) and 163.5 eV (S 2p1/2) are observed which are assigned to S^{2-}, indicating the presence of metal sulfides (CuS)[4]. Another peak at around 161.5 eV appeared after the addition of $CdCl_2$ for the XPS spectra of S 2p region, confirming the formation of metal sulfides including Cu_2S[29, 51, 52]. Moreover, the peak positions of Cu 2p1/2 at 951.9 eV and S 2p at 161.5 eV are slightly shifted to lower binding energy region with the increase of $CdCl_2$ content, indicating the existence of more Cu^+ on the surface in Cd-0.5, Cd-1, Cd-2, and Cd-4. In addition,
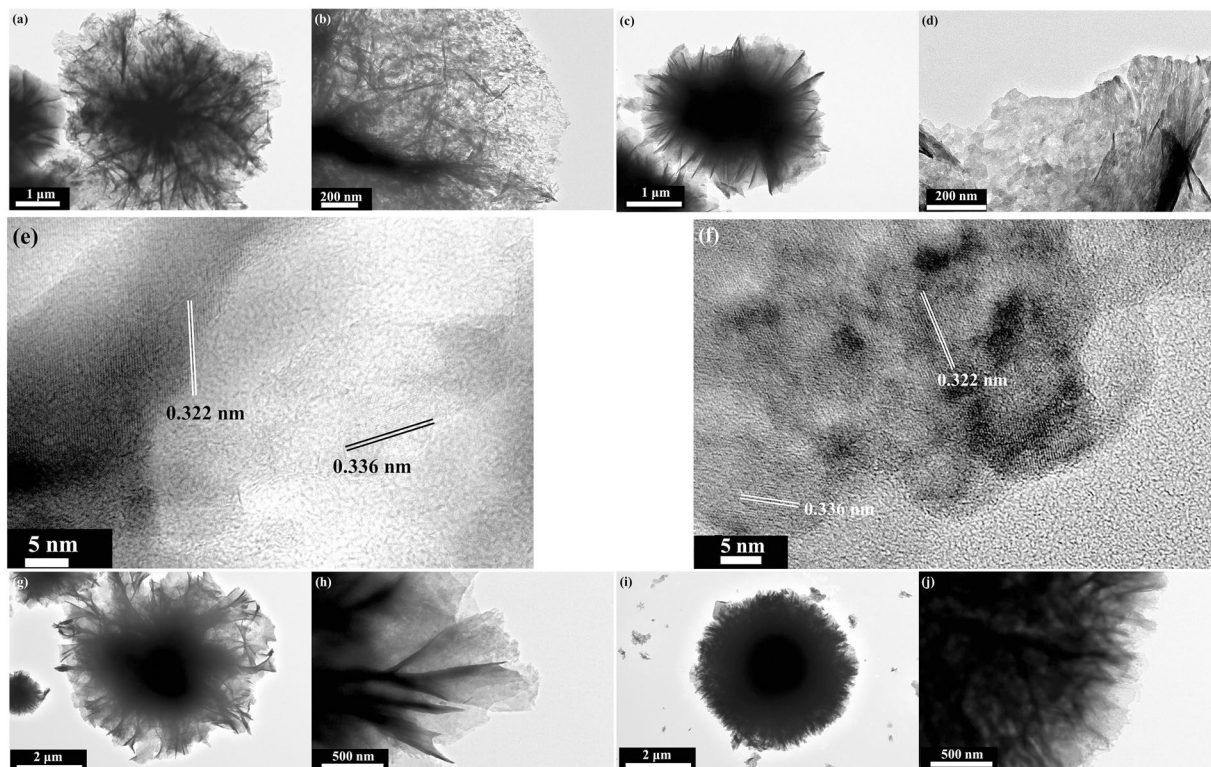
Figure 6. Typical TEM images of as-prepared samples with corresponding high magnification: (**a,b**) Cd-1, (**c,d**) Cd-2, (**g,h**) Cd-1-T4, and (**i,j**) Cd-1-T6. HRTEM images of as-prepared samples Cd-1 (**e**) and Cd-2 (**f**).
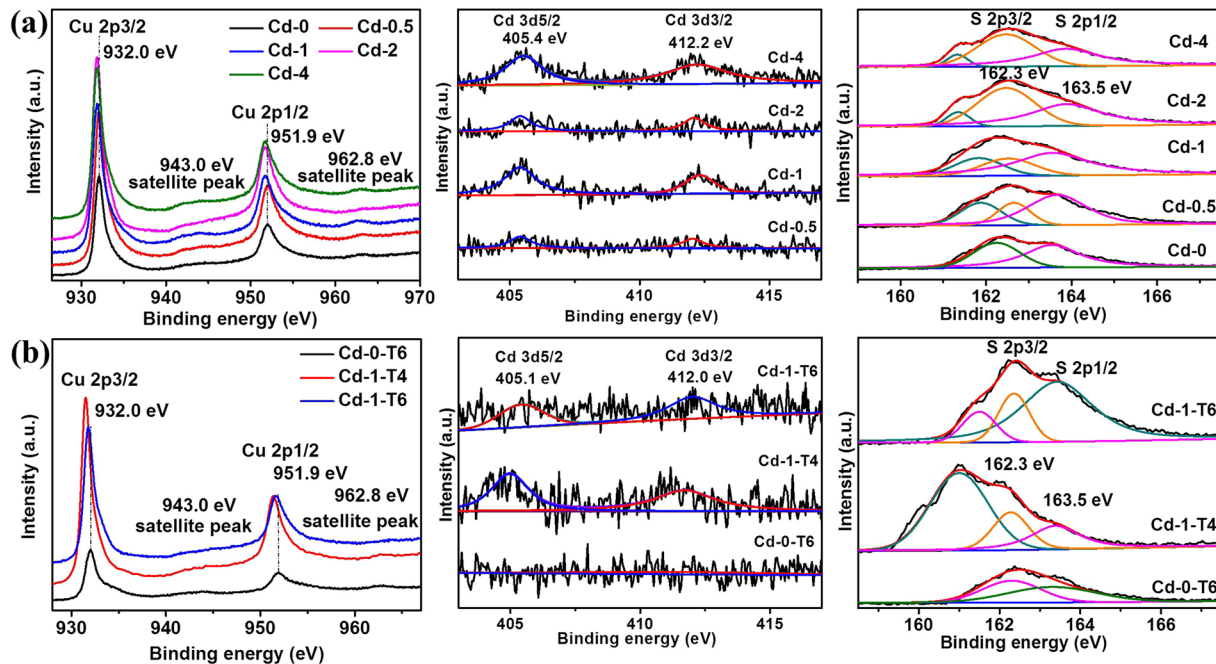

Figure 7. XPS analysis of as-synthesized samples in the Cu 2p, Cd 3d and S 2p regions. (**a**) Samples prepared by changing the amount of Cd content with fixing thiourea, and (**b**) Samples obtained by modulating the contents of both Cd and thiourea.
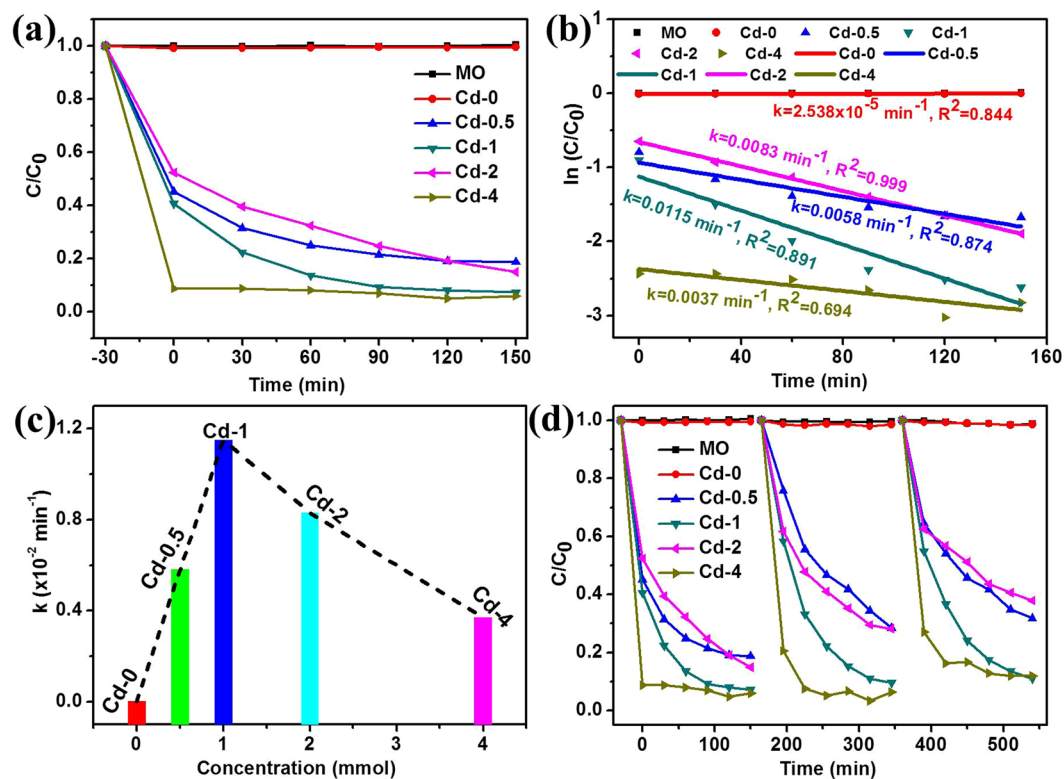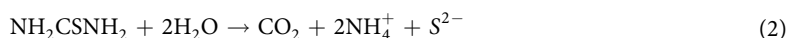
Figure 8. (**a**) Relative concentration (C/C_0) of MO versus time under visible light irradiation using the samples prepared by different amounts of $CdCl_2$. (**b**) The corresponding plots of $\ln(C/C_0)$ *vs.* time of the data in (**a**). (**c**) The kinetics plots of rate constant (k) *vs.* $CdCl_2$ concentration during the preparing process for samples Cd-0, Cd-0.5, Cd-1, Cd-2, and Cd-4. Dots and lines in (**b**) stand for original and linear fitting data, respectively. (**d**) Cycling test of all photocatalysts in the photodegradation of MO under visible light irradiation.

the peak positions of Cu 2p for Cd-1-T4 are apparently shifted to much lower binding energy region, compared with those of Cd-0-T6 and Cd-1-T6, illustrating the formation of much more Cu^+ on the surface. These results are in well agreement with the observation of S 2p region and previous reports[30, 52]. The reason for the formation of Cu_2S may be ascribed to the amount of thiourea and chloride ions from the addition of cadmium chloride in the precursor solution[45, 52–54].

The growth mechanism for the formation CdS decorated CuS could be explained based on previous reports[4, 22, 29, 45, 50–54]. Thiourea (Tu) is considered to easily coordinate with copper (II) ion in aqueous solution owing to the availability of lone pair of electrons on the ligand and free states of metallic ions[4, 22, 55]. Then thiourea-copper (II) complex could serve as Cu^{2+} precursors. The possible chemical reaction could be expressed as follows[4, 10, 55–57]:

$$Cu^{2+} + x\text{Tu} \rightarrow [Cu(\text{Tu})_x]^{2+} \tag{1}$$

$$NH_2CSNH_2 + 2H_2O \rightarrow CO_2 + 2NH_4^+ + S^{2-} \tag{2}$$

$$Cu^{2+} + S^{2-} \rightarrow CuS \tag{3}$$

$$Cd^{2+} + S^{2-} \rightarrow CdS \tag{4}$$

The different products solubility of CdS (8×10^{-28}) and CuS (6.3×10^{-36}) would generate the preferential formation of CuS followed by CdS, which generate the CdS decorated CuS structure[51]. The appearance of Cu_2S after the addition of cadmium chloride ($CdCl_2$) mainly caused by the introduction of chloride anion (Cl^-) with the assist of polyethylene glycol under hydrothermal condition, which have been reported by other groups[45, 53, 54, 58]. The higher concentration of chloride ions in the precursor solution facilitates the formation of Cu_2S, interpreting the aforementioned tendency of binding energy shift. When more thiourea was added into the precursor solution, the amount of Cu_2S phase decreases, which could be explained using the following reaction[53, 59]:
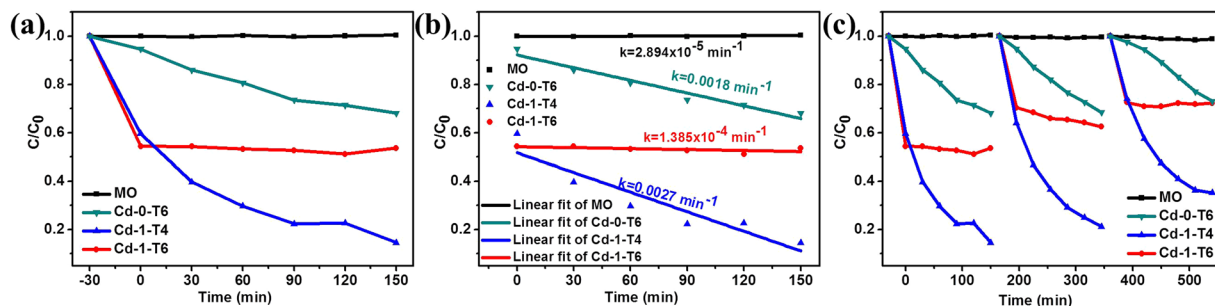
$$Cu_2S + S^{2-} \rightarrow 2CuS + 2e^- \tag{5}$$

Figure 9. (**a**) Phtotodegradation of MO over as-prepared samples under visible light irradiation. (**b**) The first-order kinetic plot of $\ln(C/C_0)$ *vs*. time corresponding to the data in (**a**). (**c**) Catalysts recycling in the photodegradation of MO.

Photocatalytic properties.

The photocatalytic activities of the as-prepared samples towards the degradation of MO were evaluated under visible light irradiation (UV-vis spectral variations of MO in aqueous solution were shown in Supporting Information Fig. SI-3). Figure 8a shows that the samples prepared by different $CdCl_2$ concentrations have diverse photocatalytic activities. The lowest photodegradation efficiency was observed by the sample Cd-0 with no photodegradation of MO has been found, which could be attributed to the effect of morphology[4, 25]. After addition $CdCl_2$, the photocatalytic activities were obviously enhanced. Sample Cd-4 shows the highest adsorption activity towards MO and only 9% MO remain after 30 min in dark. However, the photo-degradation efficiency was not follow the sequence with the increase of $CdCl_2$ content, which can be obviously observed from the photocatalytic degradation kinetics as shown in Fig. 8b and c. The photocataytic degradation kinetics of MO by using our synthesized catalysts were analyzed by the pseudo first-order model to determine the rate constant of photodegradation with respect to the degradation time when the initial concentration of the pollutant is low, as the following equation[4, 8, 16]:

$$\ln(C/C_0) = -kt \tag{6}$$

where C_0 is the initial concentration of MO, C is the concentration at time t, and k is the reaction rate constant. The rate constant was estimated by the slopes of linear fit as depicted in Fig. 8b and the relationship between the reaction rate constant and $CdCl_2$ concentration was plotted in Fig. 8c, showing that Cd-1 with the suitable $CdCl_2$ concentration can achieve the optimal photodegradation efficiency. The durability of the samples was evaluated by cycle measuring the photodegradation efficiency of MO aqueous solution and again Cd-1 possesses the best durability than others (Fig. 8d). For comparison, the photocatalytic activities of other samples including Cd-0-T6, Cd-1-T4, and Cd-1-T6 were also investigated under the same conditions. Form Fig. 9a and b, it can be seen that Cd-1-T4 exhibits the largest reaction rate constant and Cd-0-T6 possesses the lowest photodegradation efficiency, while sample Cd-1-T6 only shows the absorption ability of MO. Meanwhile, the stability of sample Cd-1-T4 becomes worse after 3 times recycling test as shown in Fig. 9c.

In order to explore the underlying photodegradation reaction mechanism of the synthesized catalysts, the morphological and XPS measurement were once again conducted for typical samples. The TEM images for samples Cd-1 and Cd-2 (Fig. 10a–d), confirmed that no significant differences occurred after photodegradation of MO aqueous solution under visible light irradiation compared with the pristine structures. In addition, XPS spectra for samples Cd-0, Cd-0.5, Cd-1, and Cd-2 also confirmed no obvious changes after photodegradation compared with the data before photocatalytic test (Figs 10e–g, and SI-4). All these results demonstrate the super stable manner of the as-prepared samples for photodegradation of MO.

Based on the above characteristic results, the photocatalytic reaction mechanism could be proposed as follows: (1) the individual CuS or CdS can generate photo-induced electron-hole pairs, however, they can recombine easily which results in the drastically decreased photocatalytic performance[3, 33]; (2) the specific surface area could significantly influence the photodegradation efficiency by affording different amount of active sites[28]; (3) the formation of heterojunction structure could effectively facilitate the separation of photo-induced electron-hole pairs, thus resulting in the enhanced photocatalytic activity[60]; (4) the growth of Cu_2S on the surface of as-prepared samples could not only lead to the formation of the heterojunction structure with CuS and CdS, but also provide unique structure to promote the photocatalytic activity. Therefore, the enhanced photocatalytic properties of the obtained photocatalysts could be reasonably explained as follows. Firstly, the photodegradation rate increment almost follows the trend of the enlarged specific surface area as summarized in Table 2 (N_2 adsorption-desorption isotherms of the products were shown in Supporting Information Fig. SI-5), except for samples Cd-0.5, Cd-1, and Cd-2, which may be ascribed to the increased porosity as observed from SEM and TEM images and consistent with the previously reported result[28]. Secondly, with the increase of $CdCl_2$ content, the photodegradation efficiency shows the peak shape illustrating that the higher recombination of electron-hole pairs occurred for the individual metal sulfide product. Thirdly, more CdS on the catalyst surfaces will lead to the decreased photocatalytic activity, which may be partly attributed to lower light absorption properties (see Supporting Information Fig. SI-6) due to the theoretically smaller band gap of CuS (2.08 eV) in comparison with CdS (2.4 eV)[27, 28]. Finally, the schematic diagram of the heterojunction formation that could accelerate the photodegradation was drawn and shown in Fig. 11. As seen from Fig. 11a, the photogenerated electrons in the conduction band (CB) of CuS

Sample	Cd-0	Cd-0.5	Cd-1	Cd-2	Cd-4	Cd-0-T6	Cd-1-T4	Cd-1-T6
S_{BET} (m^2/g)	1.704	38.618	31.701	35.837	21.679	2.339	24.095	20.966

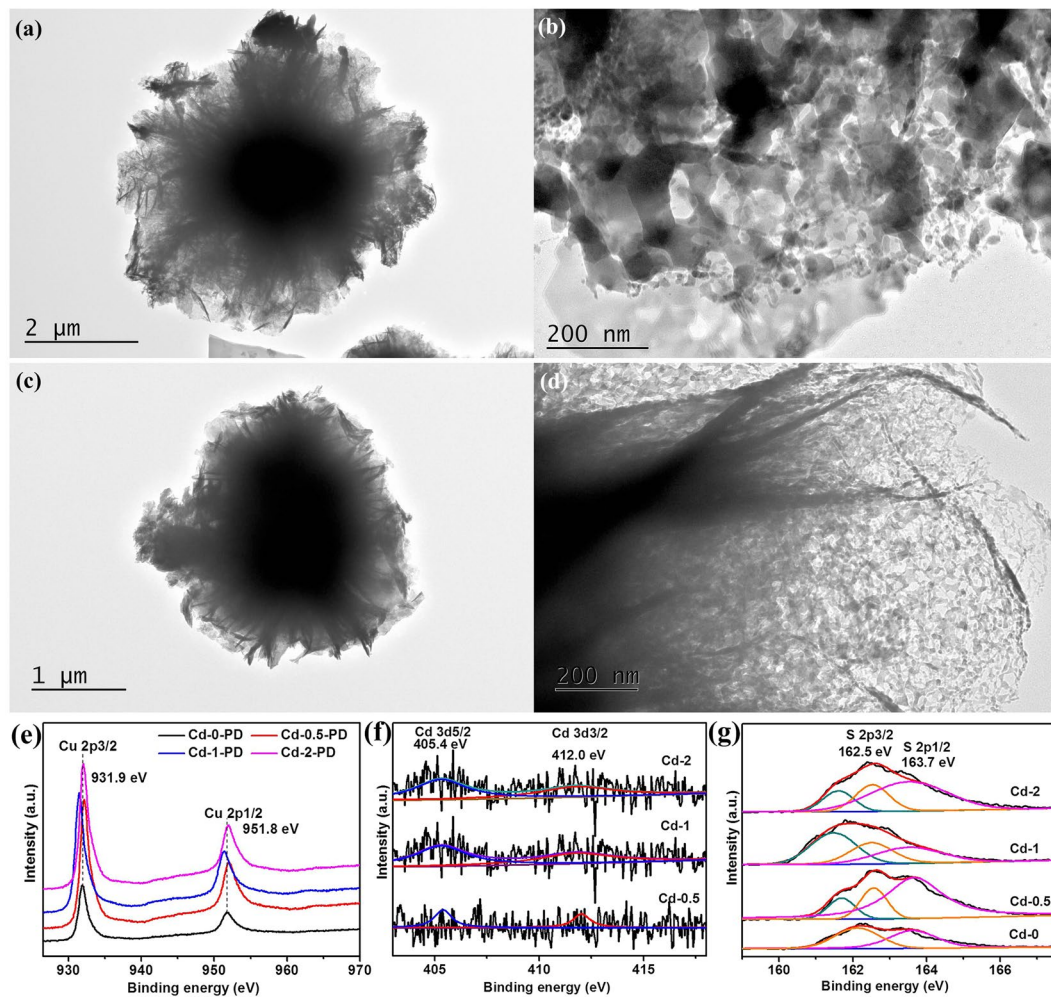**Table 2.** Summary of the specific surface area (S_{BET}) of the representative samples.

Figure 10. TEM images ((**a**,**b**) Cd-1 and (**c**,**d**) Cd-2) and (**e**–**g**) XPS analysis (including Cu 2p, Cd 3d, and S 2p spectrum) of as-prepared samples after photodegradation of MO under visible light irradiation, respectively.
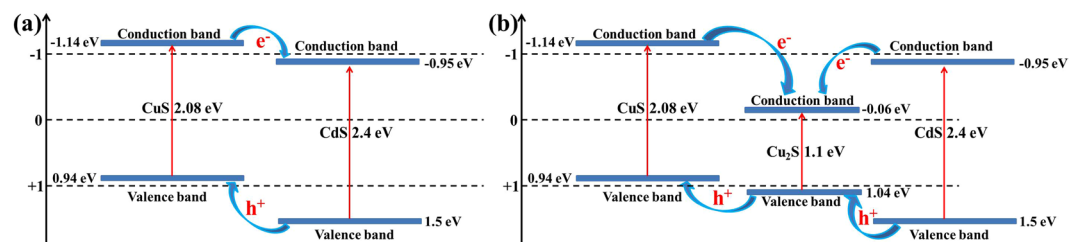

Figure 11. Schematic illustration of the band energy level and charge transfers for (**a**) CuS-CdS and (**b**) CuS-Cu$_2$S-CdS photocatalysts.

tend to easily transfer to the CB of CdS due to the driving force offered from the decreased potential energy[4, 21, 22, 27, 60], and this will lead to the formation of superoxygen radicals ($\cdot O_2$) as a result of the combination of electrons and absorbed O_2 on the surface of CdS. Meanwhile, the photogenerated holes will transfer to CuS from CdS and hydroxyl radicals ($\cdot OH$) is produced. Finally, the dyes (MO) could be effectively decomposed by these generated highly oxidant species[8, 60]. To be specific, the formed heterojunction structure could significantly reduce the electron-hole recombination rate and enhance the mobility of electrons, finally promoting the photocatalytic activities. It should be noted that the formation of Cu_2S on the surface of CuS could change the transfer behavior of electrons and holes as shown in Fig. 11b. Therefore, we proposed the decomposition of MO following a similar process by using CuS-CdS as photocatalyst. However, Cu_2S, with a small band gap, increases the possibility of light absorption in the visible range[60]. The larger gap of conduction band energy between metal sulfides generating the more smoothly transfer of photoinduced electrons restrains the recombination of electron-hole pairs[3]. Thus, the formation of Cu_2S could further enhance the photodegradation efficiency. However, it is worthwhile to note that dyes decomposition using photocatalysts is a complicated process, and many factors should be considered together as well as the photodegradation of MO in this work.

Conclusions

In summary, CdS decorated CuS microflowers were successfully synthesized by one-pot hydrothermal method. The structural and morphological investigation proved that the amount of chloride ions (from $CdCl_2$) and thiourea content during the synthetic process would significantly affect the composition and morphological transformation of as-prepared samples. The addition of cadmium chloride ($CdCl_2$) made the irregular morphologies transform to flower-like structures due to the introduction of Cl^- ions as well as the formation of CdS/CuS heterojunctions. Meanwhile, the more content of thiourea could conduct the morphological transformation from irregular to more regular with the porosity decrease and thickness increase while the more Cl^- ions addition exhibited the similar effect. The photocatalytic activity confirmed that the possible mechanism on the photodegradation of MO could be related to the following factors: the composition, specific surface area, the adsorption of radiation, and the structural and morphological character of as-prepared samples. The sample Cd-1 showed the highest photocatalytic activities on the degradation of MO, elucidating that the optimal synthetic conditions with the suitable addition of cadmium chloride and thiourea was critical to the final photocatalytic properties. The post-photodegradation analysis illustrated that the as-prepared samples were stable for the photodegradataion of MO. The results demonstrated the potential application of CdS decorated CuS microflowers in the wastewater treatment.

References

1. Fujishima, A. & Honda, K. Electrochemical photolysis of water at a semiconductor electrode. *Nature* **238**, 37–38 (1972).
2. Chen, C. C., Ma, W. H. & Zhao, J. C. Semiconductor-mediated photodegradation of pollutants under visible-light irradiation. *Chem. Soc. Rev.* **39**, 4206–4219 (2010).
3. Chen, X. *et al*. Facile fabrication of novel porous graphitic carbon nitride/copper sulfide nanocomposites with enhanced visible light driven photocatalytic performance. *J. Colloid Interf. Sci.* **476**, 132–143 (2016).
4. Tanveer, M. *et al*. Synthesis of CuS flowers exhibiting versatile photo-catalyst response. *New J. Chem.* **39**, 1459–1468 (2015).
5. Xu, X. J., Zhai, T. Y., Shao, M. H. & Huang, J. Z. Anodic formation of anatase TiO_2 nanotubes with rod-formed walls for photocatalysis and field emitters. *Phys. Chem. Chem. Phys.* **14**, 16371–16376 (2012).
6. Park, J. C., Kim, J. H., Kwon, H. S. & Song, H. J. Gram-scale synthesis of Cu_2O nanocubes and subsequent oxidation to CuO hollow nanostructures for lithium-ion battery anode materials. *Adv. Mater.* **21**, 803–807 (2009).
7. Basnet, P. & Zhao, Y. P. Tuning the Cu_xO nanorod composition for efficient visible light induced photocatalysis. *Catal. Sci. Technol.* **6**, 2228–2238 (2016).
8. Deng, X. L., Wang, C. G., Shao, M. H., Xu, X. J. & Huang, J. Z. Low-temperature solution synthesis of CuO/Cu_2O nanostructures for enhanced photocatalytic activity with added H_2O_2: synergistic effect and mechanism insight. *RSC Adv.* **7**, 4329–4338 (2017).
9. Jiang, W. *et al*. Photocatalytic performance of Ag_2S under irradiation with visible and near-infrared light and its mechanism of degradation. *RSC Adv* **5**, 24064–24071 (2015).
10. Kundu, J. & Pradhan, D. Controlled synthesis and catalytic activity of copper sulfide nanostructured assemblies with different morphologies. *ACS Appl. Mater. Interfaces* **6**, 1823–1834 (2014).
11. Ma, L. S. *et al*. Controlled assembly of Bi_2S_3 architectures as Schottky diode, supercapacitor electrodes and highly efficient photocatalysts. *RSC Adv.* **4**, 41636–41641 (2014).
12. Kriegel, I. *et al*. Tuning the excitonic and plasmonic properties of copper chalcogenide nanocrystals. *J. Am. Chem. Soc.* **134**, 1583–1590 (2012).
13. He, W. *et al*. Flexible and high energy density asymmetrical supercapacitors based on core/shell conducting polymer nanowires/manganese dioxide nanoflakes. *Nano Energy* **35**, 242–250 (2017).
14. Dong, F. *et al*. *In situ* construction of $g-C_3N_4/g-C_3N_4$ metal-free heterojunction for enhanced visible-light photocatalysis. *ACS Appl. Mater. Interfaces* **5**, 11392–11401 (2013).
15. Xu, X. *et al*. Synthesis of Cu_2O octadecahedron/TiO_2 quantum dot heterojunctions with high visible light photocatalytic activity and high stability. *ACS Appl. Mater. Interfaces* **8**, (91–101 (2016).
16. Deng, X. L. *et al*. Morphology transformation of Cu_2O sub-microstructures by Sn doping for enhanced photocatalytic properties. *J. Alloy. Compd.* **649**, 1124–1129 (2015).
17. Wan, X. *et al*. Morphology controlled syntheses of Cu-doped ZnO, tubular Zn(Cu)O and Ag decorated tubular Zn(Cu)O microcrystals for photocatalysis. *Chem. Eng. J* **272**, 58–68 (2015).
18. Zhao, Q. Q. *et al*. One-pot synthesis of Zn-doped SnO_2 nanosheet-based hierarchical architectures as glycol gas sensor and photocatalyst. *CrystEngComm* **17**, 4394–440 (2015).
19. Fu, K., Huang, J. Z., Yao, N. N., Xu, X. J. & Wei, M. Z. Enhanced photocatalytic activity of TiO_2 nanorod arrays decorated with CdSe using an upconversion TiO_2:Yb^{3+}, Er^{3+} thin film. *Ind. Eng. Chem. Res.* **54**, 659–665 (2015).
20. Fu, K., Huang, J. Z., Yao, N. N., Xu, X. J. & Wei, M. Z. Enhanced photocatalytic activity based on composite structure with down-conversion material and grapheme. *Ind. Eng. Chem. Res.* **55**, 1559–1565 (2016).
21. Hong, E. P., Kim, D. C. & Kim, J. H. Heterostructured metal sulfide (ZnS–CuS–CdS) photocatalyst for high electron utilization in hydrogen production from solar water splitting. *J. Ind. Eng. Chem.* **20**, 3869–3874 (2014).

22. He, J., Chen, L., Yi, Z. Q., Au, C. T. & Yin, S. F. CdS Nanorods Coupled with WS₂ nanosheets for enhanced photocatalytic hydrogen evolution activity. *Ind. Eng. Chem. Res.* **55**, 8327–8333 (2016).

23. Xiong, S. L., Xi, B. J. & Qian, Y. T. CdS hierarchical nanostructures with tunable morphologies: Preparation and photocatalytic properties. *J. Phys. Chem. C* **114**, 14029–14035 (2010).

24. Guo, Y. M. *et al*. Facile synthesis of mesoporous CdS nanospheres and their application in photocatalytic degradation and adsorption of organic dyes. *CrystEngComm* **14**, 1185–1188 (2012).

25. Shu, Q. W., Lan, J., Gao, M. X., Wang, J. & Huang, C. Z. Controlled synthesis of CuS caved superstructures and their application to the catalysis of organic dye degradation in the absence of light. *CrystEngComm* **17**, 1374–1380 (2015).

26. Estrada, A. C., Silva, F. M., Soares, S. F., Coutinho, J. A. P. & Trindade, T. An ionic liquid route to prepare copper sulphide nanocrystals aiming at photocatalytic applications. *RSC Adv.* **6**, 34521–34528 (2016).

27. Saranya, M., Ramachandran, R., Samuel, E. J. J., Jeong, S. K. & Grace, A. N. Enhanced visible light photocatalytic reduction of organic pollutant and electrochemical properties of CuS catalyst. *Powder Technol.* **279**, 209–220 (2015).

28. Hosseinpour, Z., Hosseinpour, S., Maaza, M. & Scarpellini, A. Co²⁺ and Ho³⁺ doped CuS nanocrystals with improved photocatalytic activity under visible light irradiation. *RSC Adv.* **6**, 42581–42588 (2016).

29. Zhang, L. J. *et al*. Noble-metal-free CuS/CdS composites for photocatalytic H₂ evolution and its photogenerated charge transfer properties. *Int. J. Hydrogen Energy* **38**, 11811–11817 (2013).

30. Zhang, J., Yu, J. G., Zhang, Y. M., Li, Q. & Gong, J. R. Visible light photocatalytic H₂-production activity of CuS/ZnS porous nanosheets based on photoinduced interfacial charge transfer. *Nano Lett.* **11**, 4774–4779 (2011).

31. Gomathisankar, P. *et al*. Photocatalytic hydrogen production with CuS/ZnO from aqueous Na₂S + Na₂SO₃ solution. *Int. J. Hydrogen Energy* **38**, 8625–8630 (2013).

32. Gao, Z. Y. *et al*. Graphene–CdS composite, synthesis and enhanced photocatalytic activity. *Appl. Surf. Sci.* **258**, 2473–2478 (2012).

33. Khan, Z. *et al*. Visible light assisted photocatalytic hydrogen generation and organic dye degradation by CdS–metal oxide hybrids in presence of graphene oxide. *RSC Adv.* **2**, 12122–12128 (2012).

34. Ashokkumar, M. An overview on semiconductor particulate systems for photoproduction of hydrogen. *Int. J. Hydrogen Energy* **23**, 427–438 (1998).

35. Kamat, P. V. Meeting the clean energy demand: Nanostructure architectures for solar energy conversion. *J. Phys. Chem. C* **111**, 2834–2860 (2007).

36. Ryu, S. Y., Balcerski, W., Lee, T. K. & Hoffmann, M. R. Photocatalytic production of hydrogen from water with visible light using hybrid catalysts of CdS attached to microporous and mesoporous silicas. *J. Phys. Chem. C* **111**, 18195–18203 (2007).

37. Huang, Y. Y. *et al*. Photochemical growth of cadmium-rich CdS nanotubes at the air–water interface and their use in photocatalysis. *J. Mater. Chem.* **19**, 6901–6906 (2009).

38. Jin, J., Yu, J. G., Liu, G. & Wong, P. K. Single crystal CdS nanowires with high visible-light photocatalytic H2-production performance. *J. Mater. Chem. A* **1**, 10927–10934 (2013).

39. Huang, Y. *et al*. Hierarchical ultrathin-branched CdS nanowire arrays with enhanced photocatalytic performance. *J. Mater. Chem. A* **3**, 19507–19516 (2015).

40. Garg, P., Kumar, S., Choudhuri, I., Mahata, A. & Pathak, B. Hexagonal planar CdS monolayer sheet for visible light photocatalysis. *J. Phys. Chem. C* **120**, 7052–7060 (2016).

41. Wang, X. X., Liu, M. C., Zhou, Z. H. & Guo, L. J. Toward facet engineering of CdS nanocrystals and their shape-dependent photocatalytic activities. *J. Phys. Chem. C* **119**, 20555–20560 (2015).

42. Qian, S. S. *et al*. An enhanced CdS/TiO₂ photocatalyst with high stability and activity: Effect of mesoporous substrate and bifunctional linking molecule. *J. Mater. Chem.* **21**, 4945–4952 (2011).

43. Qin, N. *et al*. One-dimensional CdS/TiO₂ nanofiber composites as efficient visible-light-driven photocatalysts for selective organic transformation: Synthesis, characterization, and performance. *Langmuir* **31**, 1203–1209 (2015).

44. Wang, Q. Z. *et al*. Highly efficient photocatalytic hydrogen production of flowerlike cadmium sulfide decorated by histidine. *Sci. Rep.* **5**, 13593 (2015).

45. Kumar, P., Gusain, M. & Nagarajan, R. Synthesis of Cu₁.₈S and CuS from copper-thiourea containing precursors; Anionic (Cl⁻, NO₃⁻, SO₄²⁻) influence on the product stoichiometry. *Inorg. Chem.* **50**, 3065–3070 (2011).

46. Cheng, Z. G., Wang, S. Z., Wang, Q. & Geng, B. Y. A facile solution chemical route to self-assembly of CuS ball-flowers and their application as an efficient photocatalyst. *CrystEngComm.* **12**, 144–149 (2010).

47. Bulgakova, A. V. *et al*. The effect of the precipitation conditions on the morphology and the sorption properties of CuS particles. *Prot. Met. Phys. Chem. Surf* **52**, 448–453 (2016).

48. Sofronov, D. S. *et al*. Effect of anions and medium pH on the formation of ZnS micro- and nanoparticles from thiourea solutions. *J. Biol. Phys. Chem.* **13**, 85–89 (2013).

49. Fang, Z. *et al*. Phase evolution of Cu-S system in ethylene glycol solution: the effect of anion and PVP on the transformation of thiourea. *Chin. J. Chem.* **31**, 1015–1021 (2013).

50. Zong, X. *et al*. Photocatalytic H₂ evolution on CdS loaded with WS₂ as cocatalyst under visible light irradiation. *J. Phys. Chem. C* **115**, 12202–12208 (2011).

51. Yu, J. G., Zhang, J. & Liu, S. W. Ion-exchange synthesis and enhanced visible-light photoactivity of CuS/ZnS nanocomposite hollow spheres. *J. Phys. Chem. C* **114**, 13642–13649 (2010).

52. Kar, P., Farsinezhad, S., Zhang, X. J. & Shankar, K. Anodic Cu₂S and CuS nanorod and nanowall arrays: preparation, properties and application in CO₂ photoreduction. *Nanoscale* **6**, 14305–14318 (2014).

53. Jiang, X. C. *et al*. Preparation and phase transformation of nanocrystalline copper sulfides (Cu₉S₈, Cu₇S₄ and CuS) at low temperature. *J. Mater. Chem.* **10**, 2193–2196 (2000).

54. Lu, Q. Y., Gao, F. & Zhao, D. Y. The assembly of semiconductor sulfide nanocrystallites with organic reagents as templates. *Nanotechnology* **13**, 741–745 (2002).

55. Chen, G. Y. *et al*. Synthesis, characterization, and formation mechanism of copper sulfide-core/carbon-sheath cables by a sSimple hydrothermal route. *Cryst. Growth Des.* **8**, 2137–2143 (2008).

56. Chen, G. Y. *et al*. Hydrothermal synthesis of copper sulfide with novel hierarchical structures and its application in lithium-ion batteries. *Appl. Surf. Sci.* **277**, 268–271 (2013).

57. Liu, Y., Jin, B., Zhu, Y. F., Zhou Ma, X. Z. & Lang, X. Y. Synthesis of Cu₂S/carbon composites with improved lithium storage performance. *Int. J. Hydrogen Energy* **40**, 670–674 (2015).

58. Li, G., Liu, M. Y. & Liu, H. J. Controlled synthesis of porous flowerlike Cu₂S microspheres with nanosheet-assembly. *CrystEngComm* **13**, 5337–5341 (2011).

59. Khairy, E. M. & Darwish, N. A. Studies on copper-semiconducting layer-electrolyte systems—II. Galvanostatic anodic polarization of Cu/Cu₂S/S²⁻ applying stationary and rectangular pulse techniques. *Corros. Sci.* **13**, 149–164 (1973).

60. Tian, Q. Y. *et al*. Tube-like ternary α-Fe₂O₃@SnO₂@Cu₂O sandwich heterostructures: Synthesis and enhanced photocatalytic properties. *ACS Appl. Mater. Interfaces* **6**, 13088–13097 (2014).

Acknowledgements

Author Contributions

X.L.D., M.D., X.J.X. and J.Z.H. planned the projects and designed the experiments; X.L.D., C.G.W., and H.C.Y. carried out the experiments; X.L.D., X.J.X., and J.Z.H. analyzed the data and wrote the paper. M.H.S., S.W.Z., and X.W. contributed to the discussion of the paper. All authors read and approved the final manuscript.

Additional Information

Supplementary information accompanies this paper at doi:10.1038/s41598-017-04270-y

Competing Interests: The authors declare that they have no competing interests.

Publisher's note: Springer Nature remains neutral with regard to jurisdictional claims in published maps and institutional affiliations.